Physics of Fluids

Numerical simulation of thermochemical non-equilibrium flow-field characteristics around a hypersonic atmospheric reentry vehicle

Cite as: Phys. Fluids **34**, 126103 (2022); https://doi.org/10.1063/5.0131460
Submitted: 20 October 2022 • Accepted: 22 November 2022 • Accepted Manuscript Online: 23 November 2022 • Published Online: 08 December 2022

Minghao Yu (喻明浩), Zeyang Qiu (邱泽洋), Bowen Zhong (钟伯文), et al.

Physics of Fluids ARTICLE scitation.org/journal/phf

Numerical simulation of thermochemical non-equilibrium flow-field characteristics around a hypersonic atmospheric reentry vehicle

Cite as: Phys. Fluids **34**, 126103 (2022); doi: 10.1063/5.0131460
Submitted: 20 October 2022 · Accepted: 22 November 2022 ·
Published Online: 8 December 2022

Minghao Yu (喻明浩),[1] Zeyang Qiu (邱泽洋),[1] Bowen Zhong (钟伯文),[2,a)] and Yusuke Takahashi[3]

AFFILIATIONS

[1]Faculty of Mechanical and Precision Instrument Engineering, Xi'an University of Technology, Xi'an 710048, China
[2]School of Aircraft Engineering, Nanchang Hangkong University, Nanchang 330063, China
[3]Division of Mechanical and Space Engineering, Hokkaido University, Hokkaido 060-8628, Japan

Note: This paper is part of the special topic, Hypersonic Flow.
[a)]**Author to whom correspondence should be addressed:** zhongbowen@nchu.edu.cn

ABSTRACT

A multi-physics thermochemical non-equilibrium model is established to study the flow characteristics of the plasma sheath around an atmospheric reentry demonstrator. This model includes the tight coupling of Navier–Stokes equations, 54 chemical reactions of air, and a four-temperature model. The processes of dissociation, ionization, and the internal energy exchanges of air components were successfully simulated during aerodynamic heating of the reentry vehicle. The distributions of plasma sheath temperature, the molar fraction of air species, stagnation pressure, surface pressure, and electron number density around the reentry vehicle were obtained at different flight altitudes. Additionally, to validate the numerical model developed in this study, the flow characteristics of the Radio Attenuation Measurement-C-II (RAM-C-II) vehicle are also simulated and then compared with corresponding experimental data. They show good consistency in general. It is found that when the vehicle is at a high flight altitude, there is a strong thermochemical non-equilibrium phenomenon around the vehicle. However, the plasma sheath tends to be in local thermal equilibrium at a low flight altitude. The distance from the shock layer to the stagnation point decreases with a decrease in reentry altitude from 90 to 65 km but increases with a decrease from 65 to 40 km. The electron number density in the shock layer is maximum. The distribution of the electron number density in the wake region differs significantly at different flight altitudes.

I. INTRODUCTION

During the reentry process of a hypersonic vehicle from low-Earth orbit to the atmosphere, the radio frequency (RF) blackout between the spacecraft and ground communication stations or data satellites is one of the fundamental problems needed to be solved in the field of human spaceflight today. In the processes of entry, descent, and landing, incoming air is rapidly heated and compressed owing to the rapid reentry speed, forming an intense shock layer at the front of the spacecraft, thus promoting air dissociation and ionization reactions with obvious thermochemical non-equilibrium effects. Eventually, a high-temperature gas sheath forms, i.e., a plasma sheath. Inside the plasma sheath, there are large amounts of free electrons and cations around the aircraft's surface, enabling it to reflect, absorb, and scatter electromagnetic waves, resulting in communication interruptions, i.e., a blackout between the aeronauts and the ground control center. The high electron number density in the plasma sheath was reported as the key reason for the blackout.[1–5]

Figure 1 illustrates the formation of the plasma sheath and RF blackout of the reentry vehicle. In reality, communication interruptions have been previously observable by humans in various experiments of reentry flights, including the Radio Attenuation Measurement-C-II (RAM-C-II),[6] Mars Pathfinder,[7] Atmospheric Reentry Demonstrator (ARD),[8] and Orbital Reentry Experiment (OREX).[9] When a communication interruption occurs, the ground base station is not only unavailable to receive the flight data from the reentry vehicle but also has great difficulty tracking the location of the vehicle. Therefore, in the aerospace field, the avoidance of blackout of reentry vehicles is a high priority, because it can lead to mistakes in determining the landing location of the vehicle, high recovery costs,

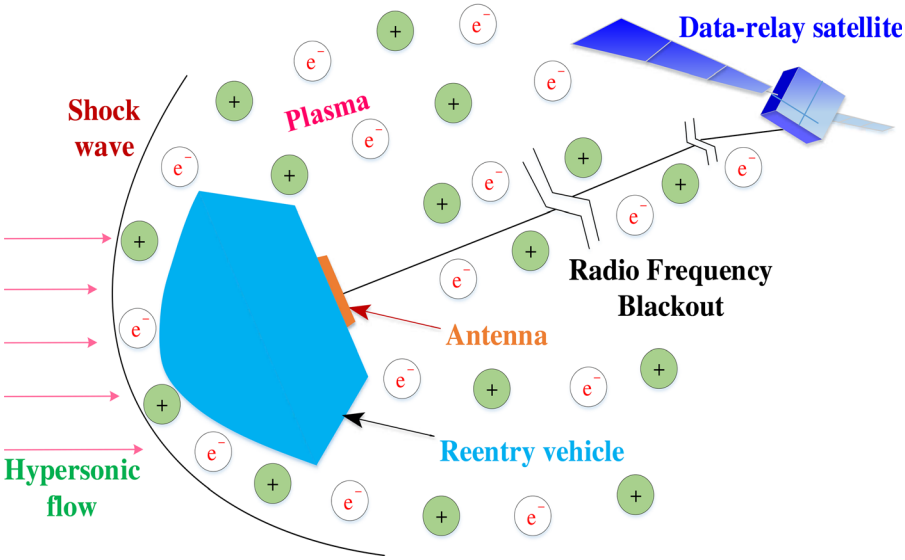

FIG. 1. Illustration of the plasma sheath and blackout of a reentry vehicle.

serious safety threats to the lives of aeronauts, and ultimately to the failure of an entire space exploration mission. Since RF blackout is highly correlated with the plasma sheath properties of the vehicle, especially the electron number density, it is necessary to reveal the complex flow characteristics of the plasma sheath before evaluating signal loss and RF blackout. However, the available ground test facilities, including hypersonic wind tunnels, not only have long experimental periods and high costs but also cannot precisely reproduce the plasma environment. With significant improvements in computer performance and the accuracy of numerical algorithms in recent decades, numerical simulation is already a useful method for researching the plasma sheath.

To date, many researchers have conducted extensive investigations on the plasma sheath of the reentry vehicle. Tchuen *et al.*[10] employed a multi-temperature Navier–Stokes model to evaluate various aerothermodynamic parameters of a vehicle with zero angle of attack in flight. They found that the effects of electron relaxation and ionization on the species concentration and temperature distribution of the vehicle plasma sheath were significant. If these factors were ignored in the simulation, they would cause distorted predictions of heat flux and chemical reactions. Takahashi *et al.* simulated the aerodynamic heating phenomena of the Hayabusa vehicle[11] and the inflatable membrane vehicle[12,13] by a combination of numerical simulation and experimental validation. They investigated the characteristics of plasma flow and expansion flow around the vehicle, respectively, as well as the ability of the flexible membrane vehicle to mitigate aerodynamic heating. Palharinl *et al.*[14] used the direct Monte Carlo method to calculate the hypersonic rarefied gas flow in a cavity, focusing on the chemistry and flow field structure in the rarefied environment and analyzing the cavity flow field structure for different length-to-depth cases. Surzhikov *et al.*[15] studied the characteristics of the ionized flow field near the RAM-C-II vehicle using a self-developed non-equilibrium flow-field simulation model and explained the resulting spatial effects. Jung[16] simulated a three-dimensional and axisymmetric model of the OREX plasma sheath. The results showed that both models could reproduce the vehicle plasma sheath flow characteristics, although some errors owing to recombination reactions were observed near the vehicle surface. Yao *et al.*[17] studied the plasma properties of the shock layer along the stagnation line by developing a high-temperature air collisional radiation model. The results showed that vibrational processes mainly control the energy transfer and the role of electron excited modes is ignorable at low altitudes and low Mach conditions. Liu[18] validated two types of chemical reaction kinetic models, which were developed by Park and Gupta, using a blunt-headed return capsule, and the results showed that both models matched the experiments in terms of capturing shock wave and pressure calculations, but the Gupta model could obtain more accurate heat flux. Hao *et al.*[19] used a three-temperature model to investigate the effect of electron energy non-equilibrium on the characteristics of a hypersonic flow field. The results showed that the energy modes rapidly equilibrate and that the electron-energy non-equilibrium does not influence the flow heat transfer between the surfaces at very high temperatures. Liang[20] studied the problem of the radiative properties caused by high-temperature gases based on flow field simulation of hypersonic vehicles, focusing on two types of high-temperature gas radiation modeling and calculation problems, namely, equilibrium radiation and non-equilibrium radiation. In the non-equilibrium radiation case, the absorption and emission decrease with increased flight altitude.

In this study, the ARD is used as the research object to establish a multi-field coupled model that accurately predicts the variation of the plasma sheath parameters of the reentry vehicle. A numerical iterative method is used to solve the Navier–Stokes equations, coupled with the thermodynamic non-equilibrium model and the 54 chemical kinetic model. Through the simulation of high-temperature ionization and internal energy exchange during the aerodynamic heating of the vehicle, the variation of electron number density, particle molar fraction, pressure, and electron temperature in the plasma sheath of the vehicle

under different altitude conditions are obtained. This study provides basic data and theoretical guidance for predicting the flow characteristics of the plasma sheath of a reentry vehicle.

II. PHYSICAL MODEL AND COMPUTATIONAL DOMAIN

The ARD is an Apollo-like blunt-head return capsule with 70% of the volume of the Apollo vehicle, the geometry is shown in Fig. 2. The main components of the vehicle are the head shield, the rear cone, and the rear cover.[21] The head shield is a hemispherical structure with a radius of 3360 mm, which is connected to the rear cone with an inclination angle of 33° through a shoulder with a cross-sectional radius of 140 mm. The maximum projected diameter of the shield is 2800 mm.

In 1998, the European Space Agency used the Ariane 5 V503 rocket to send the ARD into its target orbit in space and separated it by using the ejection mechanism. The ARD relied on its inertia to reach the top of its intended orbit before reentry into the atmosphere of Earth. Eventually, the ARD dropped into the Pacific Ocean at a speed of 6.7 m/s owing to the action of atmospheric friction and an onboard parachute.[22]

A total of six antennas are installed in the rear cone and are responsible for communication with the tracking and data relay satellite (TDRS), the global positioning system (GPS). The GPS and TDRS operate at 1.575 and 2.267 GHz, respectively.[23] During the actual reentry of the ARD to Earth, measurements of the altitude at the beginning and end of the communication blackout and the electromagnetic wave amplitude revealed that although there was a serious RF blackout of the GPS link from 90 to 40 km, the TDRS link has a strong electromagnetic attenuation phenomenon from 86 to 44 km, no RF blackout was observed. It is difficult to evaluate the blackout phenomenon through numerical simulations because of the long duration of GPS link disruption. Therefore, the TDRS link is an ideal tool to study the electron number density in the reentry flow field, and its installation position is shown in Fig. 2. The critical electron number density causing RF disruption can be calculated according to the TDRS link frequency[24]

$$f_{TDRS} = \frac{\omega_p}{2\pi} = \frac{1}{2\pi}\sqrt{\frac{e^2 n_{e,crit}}{\epsilon_0 m_e}}, \tag{1}$$

where f_{TDRS} represents the TDRS link frequency; $n_{\mathrm{e,crit}}$ represents the critical electron number density causing the RF blackout; and e, m_e, and ϵ_0 represent the fundamental charge, electron mass, and free space permittivity, respectively.

The axisymmetric computational grid of the ARD at 85 km in this paper is shown in Fig. 3. A similar flow field grid is used for the rest of the altitude. The flow field computational domain is $-10^{-3}\,\mathrm{mm} \le x \le 10^{4}\,\mathrm{mm}$, $0\,\mathrm{mm} \le y \le 6000\,\mathrm{mm}$ and consists of 141×170 grid nodes. To accurately capture the shock layer and simulate the flow-field properties, the grid is optimized for the head of the vehicle and the area near the shock layer.

III. GOVERNING EQUATIONS AND NUMERICAL METHODS

A. Flow-field equations

To simplify the calculation, it is assumed that (1) the flow gas air is composed of 79% N_2 and 21% O_2; (2) the flow field is thermochemically non-equilibrium; (3) the flow meets the conditions of stability, continuity, and axisymmetry; (4) a four-temperature model (translational, vibration, rotation, and electron temperature) is used for the temperature of the flow field; and (5) the effects of surface catalysis, ablation, radiation, and turbulence are ignored in the calculation.

Based on the above assumptions, the numerical simulation of the plasma sheath requires not only the coupling of the total mass, momentum, and energy conservation equations but also the vibration, rotation, and electron energy conservation equations of the gas microscopic particles and the air chemistry reaction kinetics model. The final numerical model is a system of thermochemical non-equilibrium hydrodynamic equations, thus

$$\frac{\partial \boldsymbol{Q}}{\partial t} + \frac{\partial \boldsymbol{F}}{\partial x_j} = \frac{\partial \boldsymbol{F}_v}{\partial x_j} + \boldsymbol{W}. \tag{2}$$

The conservation variables $\boldsymbol{Q}$, the inviscid flux $\boldsymbol{F}$, the viscous flux $\boldsymbol{F}_v$, and the source term $\boldsymbol{W}$ in Eq. (2) are represented by the following matrix vectors. The first to seventh rows of the matrix equations represent the total mass, momentum, total energy, mass of particle $\boldsymbol{s}$, rotational energy, vibrational energy, and electron energy conservation equations, respectively,

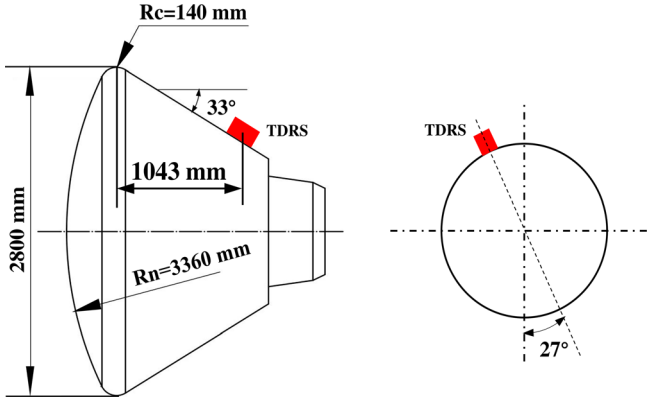

FIG. 2. Geometry of the ARD.

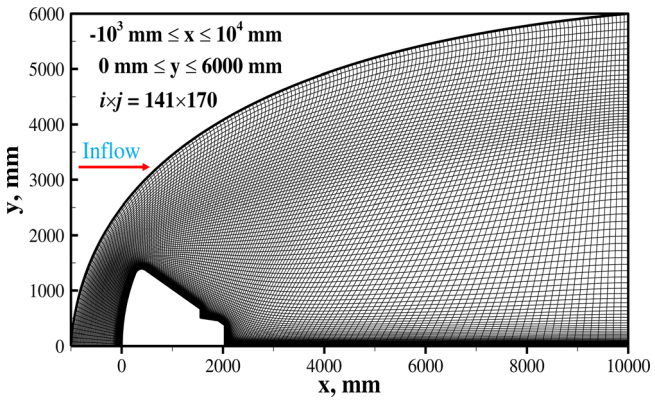

FIG. 3. The axisymmetric calculation grid of the ARD at an altitude of 85 km.

$$\boldsymbol{Q}=\begin{bmatrix}\rho\\ \rho u_i\\ E\\ \rho_s\\ E_{\mathrm{rot}}\\ E_{\mathrm{vib}}\\ E_{\mathrm{e}}\end{bmatrix},\quad \boldsymbol{F}=\begin{bmatrix}\rho u_j\\ \rho u_i u_j+\delta_{ij}p\\ (E+p)u_j\\ \rho_s u_j\\ E_{\mathrm{rot}}u_j\\ E_{\mathrm{vib}}u_j\\ E_{\mathrm{e}}u_j\end{bmatrix},$$

$$\boldsymbol{F}_v=\begin{bmatrix}0\\ \tau_{ij}\\ -q_j+u_j\tau_{ij}\\ \rho D_s\dfrac{\partial X_s}{\partial x_j}\\ -q_{\mathrm{rot},j}\\ -q_{\mathrm{vib},j}\\ -q_{\mathrm{e},j}-p_{\mathrm{e}}u_j\end{bmatrix},\quad \boldsymbol{W}=\begin{bmatrix}0\\ 0\\ 0\\ \dot{\omega}_s\\ S_{\mathrm{int,rot}}\\ S_{\mathrm{int,vib}}\\ S_{\mathrm{int,e}}\end{bmatrix}, \tag{3}$$

where δ_{ij} represents the Kronecker delta. D_s and X_s represent the diffusion coefficient and molar fraction of species s, respectively, which can be calculated by the equations given by Curtiss and Hirschfelder.[25] $\dot{\omega}_s$ represents the mass-production rate of species s. S_{int} represents the internal energy exchange rate. u_i (or u_j) and x_j represent the velocity and the right-angle coordinate system tensor, respectively.

The viscous stress tensor τ_{ij} is calculated as follows:

$$\tau_{ij}=\mu\left(\frac{\partial u_i}{\partial x_j}+\frac{\partial u_j}{\partial x_i}-\frac{2}{3}\frac{\partial u_k}{\partial x_k}\delta_{ij}\right), \tag{4}$$

where μ represents the viscosity. The total heat flux q_j can be described by

$$q_j=-\lambda_{\mathrm{tr}}\frac{\partial T_{\mathrm{tr}}}{\partial x_j}-\lambda_{\mathrm{rot}}\frac{\partial T_{\mathrm{rot}}}{\partial x_j}-\lambda_{\mathrm{vib}}\frac{\partial T_{\mathrm{vib}}}{\partial x_j}-\lambda_{\mathrm{e}}\frac{\partial T_{\mathrm{e}}}{\partial x_j}+\sum_s^{ns}\rho_s h_s V_s^j, \tag{5}$$

where T_{tr}, T_{rot}, T_{vib}, and T_{e} represent the translational temperature, rotational temperature, vibrational temperature, and electronic temperature, respectively. λ_{tr}, λ_{rot}, λ_{vib}, and λ_{e} represent the translational, rotational, vibrational, and electron components of the thermal conductivity, respectively. The first three of these can be calculated by the Yos formula[26,27] and λ_{e} is calculated by the third-order Sonine polynomial.[28–30]

The gas pressure p is given by

$$p=\sum_s^{ns}p_s=\sum_{s\neq e}^{ns-1}\rho_s R_s T_{tr}+\rho_{\mathrm{e}}R_{\mathrm{e}}T_{\mathrm{e}}=\rho\hat{R}T_{\mathrm{tr}}+p_{\mathrm{e}}, \tag{6}$$

where ρ_s, ρ_{e} represent the density of species s and charge density, respectively. R_s represents the gas constant. The total internal energy E is calculated by the following:

$$E=E_{\mathrm{tr}}+E_{\mathrm{rot}}+E_{\mathrm{vib}}+E_{\mathrm{e}}+\sum_s^{ns}\rho_s\Delta h_s^0+\frac{1}{2}\rho u_i u_i, \tag{7}$$

where E_{tr}, E_{rot}, E_{vib}, and E_{e} represent the translational, rotational, vibrational, and electron energies, respectively, which are expressed as follows:

$$E_{\mathrm{tr}}=\sum_{s\neq e}^{ns}\frac{3}{2}\rho_s R_s T_{\mathrm{tr}}, \tag{8}$$

$$E_{\mathrm{rot}}=\sum_{s=M}^{nm}\rho_s R_s T_{\mathrm{rot}}, \tag{9}$$

$$E_{\mathrm{vib}}=\sum_{s=M}^{nm}\frac{\rho_s R_s\Theta_{\mathrm{vib},s}}{\exp\left(\Theta_{\mathrm{vib},s}/T_{\mathrm{vib}}\right)-1}, \tag{10}$$

$$E_{\mathrm{e}}=\frac{3}{2}\rho_{\mathrm{e}}R_{\mathrm{e}}T_{\mathrm{e}}, \tag{11}$$

where $\Theta_{\mathrm{vib},s}$ represents the characteristic temperature of the vibration.

B. Chemical reactions model

To accurately simulate the dissociation, ionization, molecular recombination, and other chemical reactions occurring in the plasma sheath of the reentry vehicle under high-temperature conditions,[31] as shown in Fig. 4, this paper proposes to use the complex chemical non-equilibrium kinetic model, which contains 11 air species (N_2, O_2, NO, N_2^+, O_2^+, NO^+, N, O, N^+, O^+, and e^-) and 54 chemical reactions. The types of species and chemical reactions are listed in Table I.

The mass production rate of a species $\dot{\omega}_s$ can be calculated by the following equation:[35,36]

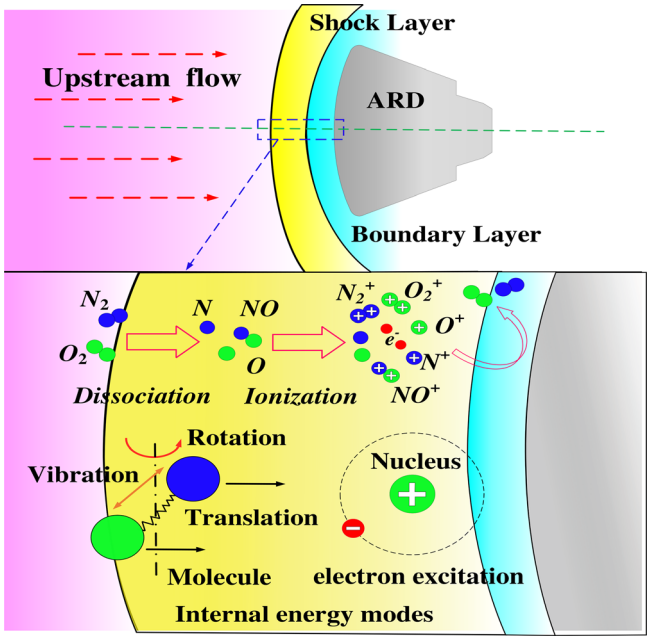

FIG. 4. Internal energy exchange and chemical reactions in the plasma sheath of the reentry vehicle.

TABLE I. 54 chemical reactions of air. $M_1 = N_2, O_2, NO, N_2^+, O_2^+, NO^+$; $M_2 = N, O, N^+, O^+$; $M_3 = N_2, O_2, N_2^+, O_2^+$; $M_4 = NO, N, O, NO^+, N^+, O^+$ and $T_{f1} = \sqrt{T_{tr}T_{vib}}$; $T_{b1} = \sqrt{T_{tr}T_e}$.

r	Reactants		Products	T_f	T_b	C_r	n	θ_r	Reference
1–6	$N_2 + M_1$	$\rightleftharpoons$	$N + N + M_1$	T_{f1}	T_{tr}	7.0×10^{21}	−1.60	113 200	32
7–10	$N_2 + M_2$	$\rightleftharpoons$	$N + N + M_2$	T_{f1}	T_{tr}	3.0×10^{22}	−1.60	113 200	32
11–16	$O_2 + M_1$	$\rightleftharpoons$	$O + O + M_1$	T_{f1}	T_{tr}	2.0×10^{21}	−1.50	59 500	32
17–20	$O_2 + M_2$	$\rightleftharpoons$	$O + O + M_2$	T_{f1}	T_{tr}	1.0×10^{22}	−1.50	59 500	32
21–24	$NO + M_3$	$\rightleftharpoons$	$N + O + M_3$	T_{f1}	T_{tr}	5.0×10^{15}	0.00	75 500	32
25–30	$NO + M_4$	$\rightleftharpoons$	$N + O + M_4$	T_{tr}	T_{tr}	1.1×10^{17}	0.00	75 500	32
31	$NO + O$	$\rightleftharpoons$	$N + O_2$	T_{tr}	T_{tr}	8.4×10^{12}	0.00	19 450	32
32	$N_2 + O$	$\rightleftharpoons$	NO+N	T_{tr}	T_{tr}	6.4×10^{17}	−1.00	38 400	32
33	$NO^+ + O$	$\rightleftharpoons$	$N^+ + O_2$	T_{tr}	T_{tr}	1.0×10^{12}	0.50	77 200	32
34	$O^+ + NO$	$\rightleftharpoons$	$N^+ + O_2$	T_{tr}	T_{tr}	1.4×10^{5}	1.90	26 600	32
35	$NO^+ + N$	$\rightleftharpoons$	$O^+ + N_2$	T_{tr}	T_{tr}	3.4×10^{13}	−1.08	12 800	32
36	$NO^+ + O$	$\rightleftharpoons$	$O_2^+ + N$	T_{tr}	T_{tr}	7.2×10^{12}	0.29	48 600	32
37	$NO^+ + N$	$\rightleftharpoons$	$N_2^+ + O$	T_{tr}	T_{tr}	7.2×10^{13}	0.00	35 500	32
38	$O_2^+ + N$	$\rightleftharpoons$	$N^+ + O_2$	T_{tr}	T_{tr}	8.7×10^{13}	0.14	28 600	32
39	$O_2^+ + N_2$	$\rightleftharpoons$	$N_2^+ + O_2$	T_{tr}	T_{tr}	9.9×10^{12}	0.00	40 700	32
40	$O_2^+ + O$	$\rightleftharpoons$	$O^+ + O_2$	T_{tr}	T_{tr}	4.0×10^{12}	−0.09	18 000	32
41	$NO^+ + O_2$	$\rightleftharpoons$	$O_2^+ + NO$	T_{tr}	T_{tr}	2.4×10^{13}	0.41	32 600	32
42	$O^+ + N_2$	$\rightleftharpoons$	$N_2^+ + O$	T_{tr}	T_{tr}	9.1×10^{11}	0.36	22 800	32
43	$N_2 + N^+$	$\rightleftharpoons$	$N_2^+ + N$	T_{tr}	T_{tr}	1.0×10^{12}	0.50	12 200	32
44	N+N	$\rightleftharpoons$	$N_2^+ + e^-$	T_{tr}	T_{tr}	4.4×10^{7}	1.50	67 500	33
45	O+O	$\rightleftharpoons$	$O_2^+ + e^-$	T_{tr}	T_{tr}	7.1×10^{2}	2.70	80 600	33
46	N+O	$\rightleftharpoons$	$NO^+ + e^-$	T_{tr}	T_{tr}	8.8×10^{8}	1.00	31 900	33
57	$N_2 + e^-$	$\rightleftharpoons$	$N+N+e^-$	T_e	T_{b1}	3.0×10^{24}	−1.60	113 200	32
48	$N+e^-$	$\rightleftharpoons$	$N^+ + e^- + e^-$	T_e	T_e	2.5×10^{34}	−3.82	168 600	32
49	$O+e^-$	$\rightleftharpoons$	$O^+ + e^- + e^{--}$	T_e	T_e	3.9×10^{33}	−3.78	158 500	32
50	$NO^+ + O$	$\rightleftharpoons$	$NO+O^+$	T_{tr}	T_{tr}	3.63×10^{15}	−0.60	50 800	34
51	$NO^+ + N$	$\rightleftharpoons$	$NO+N^+$	T_{tr}	T_{tr}	1.00×10^{19}	−0.93	61 000	34
52	$O_2 + N_2$	$\rightleftharpoons$	$NO+NO^+ + e^-$	T_{f1}	T_e	1.38×10^{20}	−1.84	141 000	34
53	$N_2 + NO$	$\rightleftharpoons$	$N_2 + NO^+ + e^-$	T_{f1}	T_e	2.20×10^{15}	−0.35	108 000	34
54	$O_2 + NO$	$\rightleftharpoons$	$O_2 + NO^+ + e^-$	T_{f1}	T_e	8.80×10^{16}	−0.35	108 000	34

$$\dot{\omega}_s = M_s \sum_{r=1}^{nr} \left(\nu_s^{b,r} - \nu_s^{f,r}\right) \times \left[k_{f,r} \prod_{j=1}^{ns} \left(\frac{\rho_j}{M_j}\right)^{\nu_{j,r}} - k_{b,r} \prod_{j=1}^{ns} \left(\frac{\rho_j}{M_j}\right)^{\nu'_{j,r}}\right], \quad (12)$$

where M_s represents the molar mass of species s. $\nu_s^{b,r}$ and $\nu_s^{f,r}$ are the stoichiometric coefficients of products and reactants of a reaction r of a chemical species s, respectively. The forward reaction rate $k_{f,r}$ and the backward reaction rate $k_{b,r}$ for a chemical reaction r can be calculated as follows:[35]

$$k_{f,r}(T_{f,r}) = C_r T_{f,r}^n \exp\left(-\frac{\theta_r}{T_{f,r}}\right), \quad (13)$$

$$k_{b,r}(T_{b,r}) = \frac{k_{f,r}(T_{b,r})}{K_r^{eq}(T_{b,r})}, \quad (14)$$

where C_r, n, and θ_r are chemical reaction coefficients. K_r^{eq} is the equilibrium constant, which can be calculated from the curve-fitting equation.[37]

C. Internal energy exchange model

To simulate the internal energy exchange processes, the rotational energy exchange rate $S_{int,rot}$, vibrational energy exchange rate $S_{int,vib}$, and electronic energy exchange rate $S_{int,e}$ should be used as the energy source term in Eq. (2). The specific calculation method is as follows:

$$S_{int,rot} = Q_{T-R} - Q_{R-V} - Q_{R-e} + Q_D^{rot}, \quad (15)$$

$$S_{int,vib} = Q_{T-V} + Q_{R-V} + Q_{e-V} + Q_D^{vib}, \quad (16)$$

$$S_{int,e} = Q_{T-e} + Q_{R-e} - Q_{e-V} + Q_D^{e} + Q_I^{e}, \quad (17)$$

where Q_{T-R}, Q_{R-V}, Q_{R-e}, Q_{T-V}, Q_{e-V}, and Q_{T-e} represent energy transfer between the translational-rotational energy modes,[38]

rotational-vibration energy modes,[39] rotational-electron energy modes,[40] translational-vibration energy modes,[39] electron-vibration energy modes,[41] and translational-electron energy modes,[42] respectively. Q_D^{rot}, Q_D^{vib}, Q_D^{e}, and Q_I^{e} represent the energy loss of air molecules.[43]

D. Boundary conditions

For the boundary conditions of the flow field: (1) at the inflow, the velocity, temperature, and density of the freestream are used as the calculation conditions, and the specific values are obtained by the flight data of the ARD,[16] as listed in Table II. The Knudsen number K_n[22] is calculated as shown in Eq. (18). The computed Knudsen number K_n at each altitude is shown in Table II. As summary, the evaluated Knudsen numbers are less than 0.01 at all altitudes, so the fluid continuity assumption is reasonable. (2) At the outflow, the flow characteristics can be obtained by zeroth extrapolation because the flow field is at supersonic speed. (3) At the vehicle wall, it is assumed that there is no catalytic effect, no slip, and no pressure gradient. (4) At the central axis, axisymmetric boundary conditions are used.

$$K_n = \frac{\lambda}{L}, \tag{18}$$

where L represents the characteristic length of the research target. $L = 2.80$ m for the ARD.[44] λ represents the mean free path of molecules.

E. Numerical methods

To obtain the flow field characteristics of the plasma sheath, the mathematical model already developed in this paper needs to be solved numerically. For the flow field, the Navier–Stokes equations involve many conservation equations, such as the total density, momentum, and total energy equations. The finite volume method is used to discretize the governing equations. The simple low-dissipation advection upstream splitting method is introduced to evaluate the inviscid fluxes of the governing equations. The viscous terms are obtained by the second-order central difference method. Owing to the large difference in timescale between the chemical reactions and the fluid motion in the simulation of thermochemical non-equilibrium flow, this paper has combined the point-implicit method and the lower-upper symmetric Gauss–Seidel method to avoid the stiffness problem in the calculation results. For the chemical reaction equations, the finite volume method is used for discretization and the Thomas algorithm is used for the iterative solution.

TABLE II. Calculation conditions and Knudsen number for different altitudes.

Altitude (km)	Velocity (m/s)	Temperature (K)	Density (kg/m^3)	K_n
90	7545	188.3	3.46×10^{-6}	7.95×10^{-3}
85	7577	191.0	8.22×10^{-6}	3.35×10^{-3}
80	7609	195.8	1.85×10^{-5}	1.49×10^{-3}
75	7592	201.7	4.01×10^{-5}	6.86×10^{-4}
70	7452	210.9	8.83×10^{-5}	3.11×10^{-4}
65	7145	225.3	1.78×10^{-4}	1.54×10^{-4}
60	6105	242.0	3.40×10^{-4}	8.09×10^{-5}
50	4567	265.2	1.15×10^{-3}	2.39×10^{-5}
45	3323	255.6	2.25×10^{-3}	1.22×10^{-5}
40	2218	250.3	4.36×10^{-3}	6.31×10^{-6}

IV. RESULTS AND DISCUSSION

A. Flow field characteristics

Figures 5(a) and 5(b) show the temperature and air density profiles along the stagnation line of the ARD at 85 and 65 km, respectively. The translational, rotational, vibrational, and electronic temperatures are completely separated when the air crosses the shock layer at an altitude of 85 km, and there is a strong thermal non-equilibrium in the flow field. The differences between the four temperatures near the shock layer are minimized at an altitude of 65 km. This

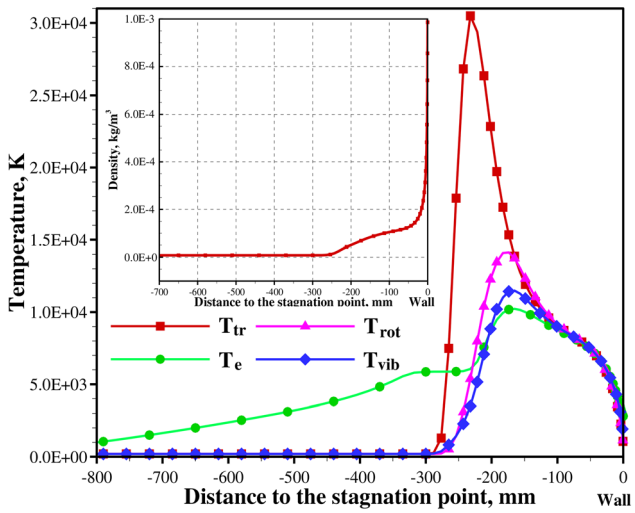

(a) Altitude of 85 km

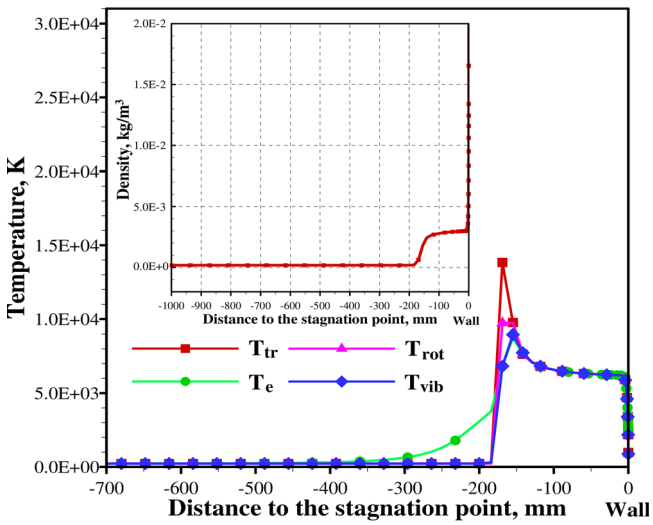

(b) Altitude of 65 km

FIG. 5. Temperature and air density profiles along the stagnation line at (a) altitude of 85 km and (b) altitude of 65 km.

is because of the different air densities and the different energy transfer rates between the internal energy models at the two altitudes. Thermal equilibrium regions are observed at both altitudes in the shock layer. It is a result of the rapid increase in air density behind the shock layer. The increased number of collisions between chemical species and the accelerated energy transfer between the internal energy models result in the chemical reactions absorbing a large amount of heat. Eventually, the temperature of the shock layer decreases. There is a big temperature gradient owing to the vehicle wall being set as an isothermal wall, whose values are far smaller than the temperature in the shock layer, so the temperature decreases rapidly near the wall.

Figures 6(a) and 6(b) show the molar fraction profiles of each species of the ARD along the stagnation line at 85 and 65 km, respectively. The rates of species reactions in the shock layer at 85 km are significantly slower than at 65 km, but the trends are similar. When the air does not pass through the shock layer, O_2 and N_2 are the main components of the inflow. The temperature of the flow field is low, no chemical reaction takes place, and the molar fraction of the two components changes slowly. The molar fraction of O_2 and N_2 molecules decrease when the inflow passes a certain point in the flow field. This is because the activation energy of the gas molecule is excited by the rapid increase in the temperature of the flow field when it passes through the shock layer, causing the dissociation of O_2 and N_2 into oxygen and nitrogen atoms, respectively. In addition, the dissociation reaction of O_2 in the shock wave proceeds faster than that of N_2 owing to the different temperatures required for the dissociation reaction of the two molecules, so the molar fraction of O_2 decreases more rapidly. The dominant chemicals are N_2, N, and O in the shock layer. With the decrease in the flow field temperature, some of the nitrogen and oxygen atoms undergo a recombination reaction to produce nitrogen and oxygen molecules, respectively, causing the molar fractions of N_2 and O_2 to rise near the wall. At the same time, the molar fraction of various ions and electrons decreases due to reduced dissociation and ionization reactions.

Figures 7(a) and 7(b) present the molar fraction distributions of N_2 and N in the flow field at 85 and 65 km, respectively. Because of the big temperature difference in the flow field around the vehicle, N_2 is more dissociated at 85 km and less dissociated at 65 km altitude. Compared with the 65 km case, N_2 in the wake region of the ARD decreases and N increases significantly in the 85 km case, and the distance from the shock layer to the stagnation point is larger. Similarly, the molar fraction distribution of O_2 and O in the flow field at both altitudes are similar.

Figure 8 shows the gas pressure profiles along the stagnation line at different altitudes, where p represents the pressure. The external frame shows the gas pressure profiles from 90 to 70 km, and the local frame shows the gas pressure profiles from 65 to 40 km. The trend of the profile is similar at all altitudes, the gas pressure rises rapidly when passing through the shock layer, slowly rises in the shock wave, and finally reaches its maximum near the vehicle wall. The maximum gas pressure increases gradually with a decrease in reentry altitude at all altitudes except 40 km, where the gas pressure does not follow the previous rule because of the reentry velocity of the vehicle at 40 km. The distance from the shock layer to the stagnation point decreases with decreasing in reentry altitude from 90 to 65 km. The distance increases with decreasing reentry altitude from 65 to 40 km, resulting from the combined effect of gas density and velocity of the vehicle.

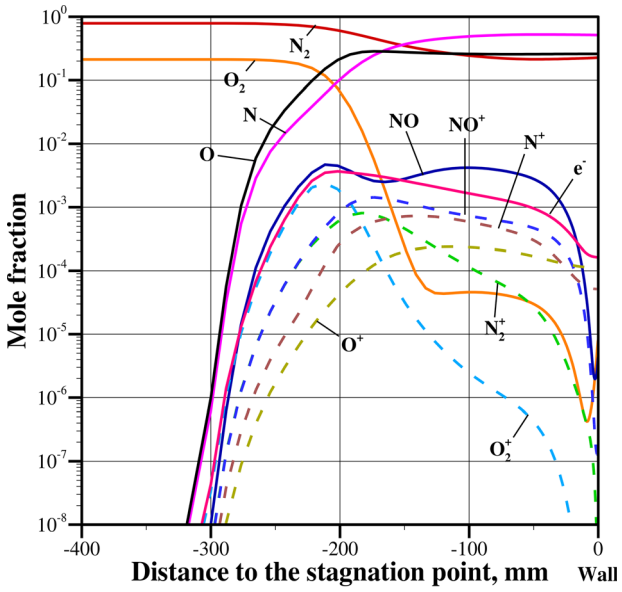

(a) Altitude of 85 km

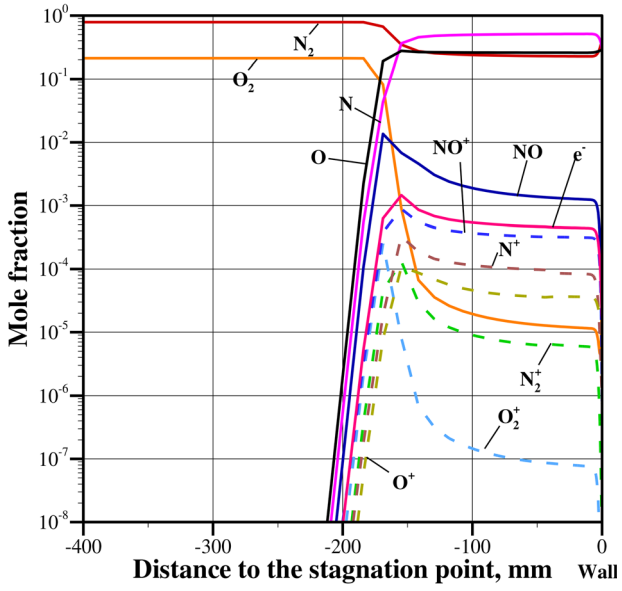

(b) Altitude of 65 km

FIG. 6. Molar fraction profiles of chemical species along the stagnation line at (a) altitude of 85 km and (b) altitude of 65 km.

Figure 9 shows the wall pressure profiles of the ARD at different altitudes. The wall high-pressure region is primarily concentrated in the vehicle head, and its value rapidly decrease in the rear cone and back cover region. When the air density gradually increases and the reentry velocity is high, the wall pressure increases with decreasing altitude. In particular, the increase trend of the wall pressure is more obvious in the head region of the vehicle. In the rear cone region and the

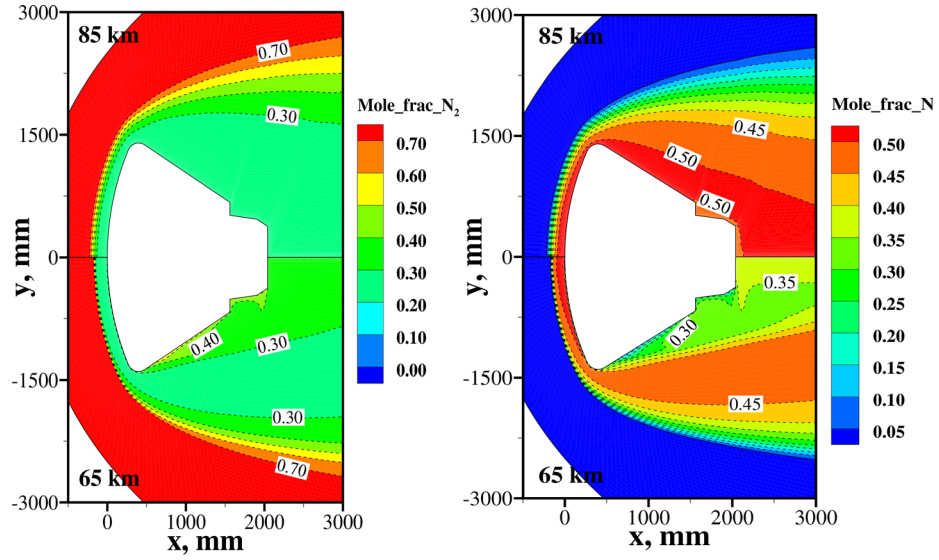

(a) Molar fraction distribution of N_2 (b) Molar fraction distribution of N

FIG. 7. Distribution of the molar fraction of N_2 and N in the flow field at (a) altitude of 85 km and (b) altitude of 65 km.

back cover region, the pressure profiles calculated at each altitude almost coincide and the difference in the values is not obvious, which means that the wall pressure in these two regions is less affected by the inflow conditions.

The distribution of electron number density in the flow field at eight different altitudes is depicted in Figs. 10(a)–10(h). The maximum value of the legend, 6.4×10^{16} m^{-3}, is the critical electron number density that would cause the RF blackout, which is calculated by substituting the TDRS link frequency into Eq. (1). The results show that, on the one hand, the electron number density in the shock layer at all eight altitudes is greater than the critical value owing to the strong shock wave. The electron number density in the wake region, on the other hand, differs significantly at different altitudes. Particularly, for the altitude range of 80–65 km, the gas density increases slightly due to the narrow convergence of the expansion flow behind the shoulder of the vehicle, increasing the electron number density in the wake region as the reentry altitude decreases. At the same time, the region where the electron number density exceeds the critical value completely blocks the ARD, so that the electromagnetic signals responsible for ground-to-space communications are attenuated, refracted, and reflected when crossing the area, resulting in a serious RF blackout. At other altitudes, either because of the thin gas at high

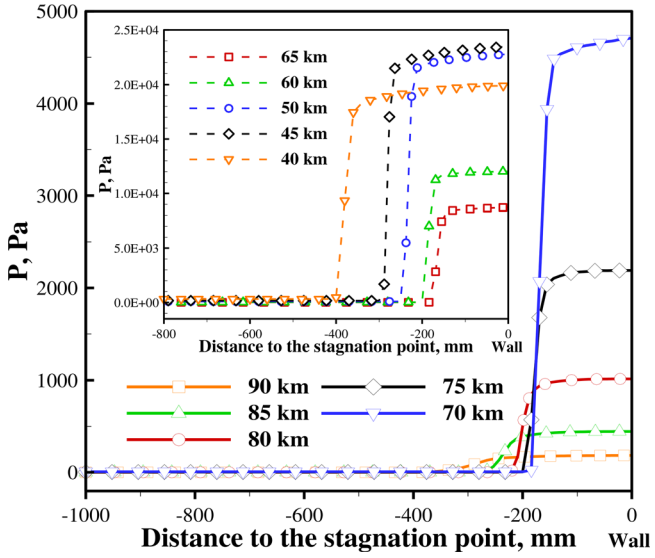

FIG. 8. Pressure profiles along the stagnation line at different altitudes.

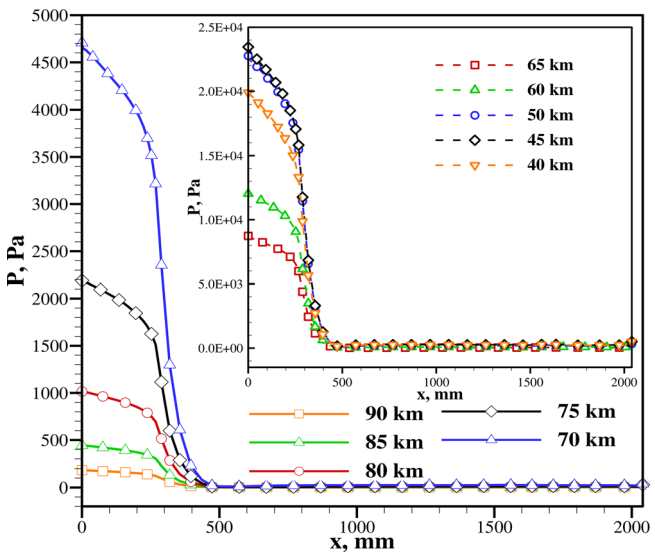

FIG. 9. Wall pressure profiles along the ARD axis at different altitudes.

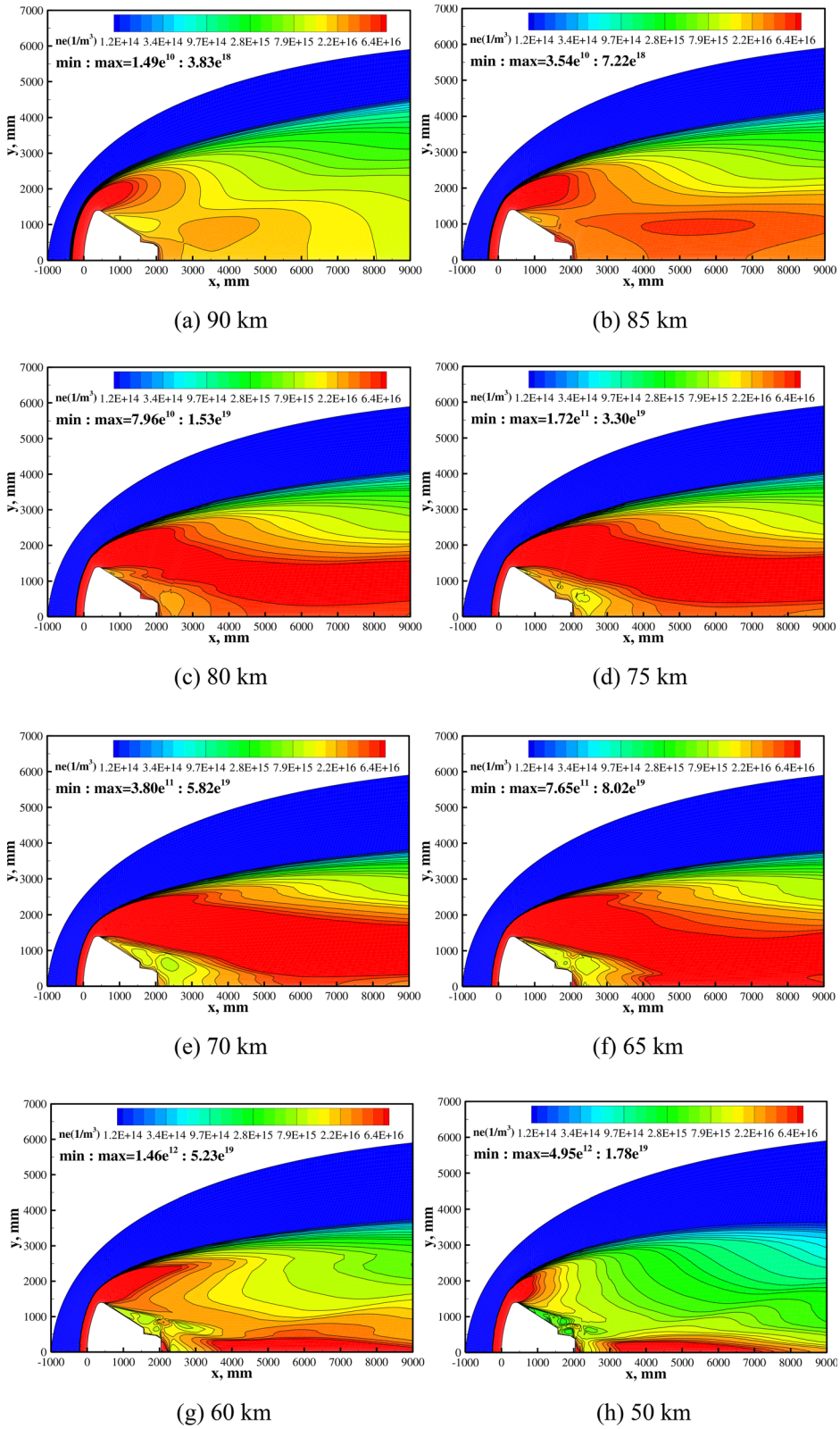

FIG. 10. Distributions of electron number density in the flow field at (a) 90, (b) 85, (c) 80, (d) 75, (e) 70, (f) 65, (g) 60, and (h) 50 km.

altitude or owing to the expansion of the inflow, the electron number density in the wake region is below the critical value, which means that the electromagnetic wave can relatively easily propagate in the wake region.

B. Comparisons of the results simulated by different chemical-reaction models

Figure 11 shows a comparison of the two chemical reaction models for the flow field parameters at 85 km. The models are the 49-reaction model[45] and the 54-reaction model for the 11 air species. The difference is that the 54-reaction model adds more ionization and electric charge exchange reactions (i.e., the $r = 50$–54 reactions in Table I) relating to NO and NO^+ to the 49-reaction model. The differences between the results of the two chemical reaction models are almost negligible in the molar fraction of chemical species along the stagnation line and electron number density in the shock layer. However, the distribution of the electron number density in the wake region differs significantly. It is clearly seen from the comparison that the electron number density in the wake region obtained from the 49-reaction model is close to the critical electron number density for the occurrence of the RF blackout and even exceeds the critical value in some areas, while the 54-reaction model obtains an electron number density that does not exceed the critical value in the wake region. The main reason for the difference is that with the supplement of NO and NO^+ related reactions, the reactions among O_2, N_2, and NO generate more NO^+, i.e., the reactions $r = 52$–54. The concentration of NO^+ increases, which promotes the reactions $r = 50$–51, leading to an accelerated consumption of O and N. Eventually, a few associative ionization reactions and electron impact ionization reactions occur. In summary, the 54-reaction model considers more associative ionization reactions ($r = 52$–54 in Table I) and more electric charge exchange reactions ($r = 50$–51 in Table I) than the 49-reaction model, the 54-reaction model has higher numerical accuracy in predicting air chemical concentrations. Therefore, the 54-reaction model has good application potential in the numerical simulation for the supersonic flow field of the reentry vehicle.

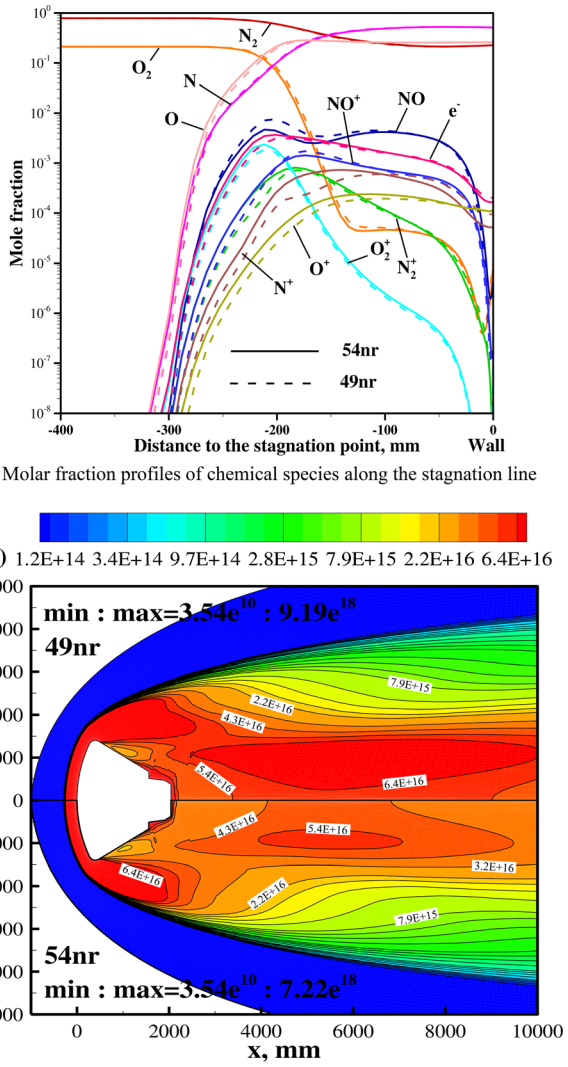

(a) Molar fraction profiles of chemical species along the stagnation line

(b) Distributions of electron number density

FIG. 11. Comparisons of the results simulated by 54 and 49 chemical-reaction models at 85 km for the ARD: (a) molar fraction profiles of chemical species along the stagnation line and (b) distributions of electron number density.

C. Model validation with experimental data

We validate and evaluate the numerical model using the electron number density test data of the published electromagnetic attenuation measurement program C (RAM-C-II) flight test.[6,46] The subject geometry is shown in Fig. 12. It is a blunt spherical cone with a spherical radius of $R_n = 0.1542$ m, a half-cone angle of $\theta = 9°$, and a total model length of $L = 1.295$ m. The computational domain of its flow field grid is $-100\ \text{mm} \le x \le 1295\ \text{mm}$, $0 \le y \le 1000$ mm and consists of 81×91 grid nodes. The flight altitudes used for the validation model are 61 and 71 km, respectively, and the initial inflow conditions are listed in Table III.

Figure 13 shows the electron number density along the RAM-C-II wall at two altitudes with different wall temperatures compared to the flight test data. The horizontal coordinate is the horizontal distance

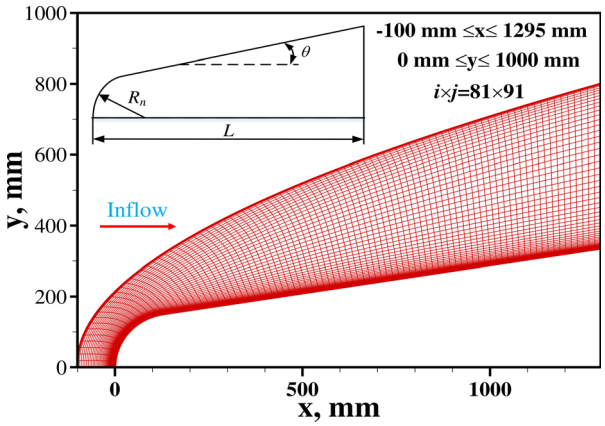

FIG. 12. Two-dimensional axisymmetric calculation grid of the RAM-C-II.

TABLE III. Free flow conditions.[20]

Altitude (km)	Ma	Velocity (m/s)	Temperature (K)	Density (kg/m^3)
61	23.9	7636	254	2.720×10^{-4}
71	25.9	7658	216	0.769×10^{-4}

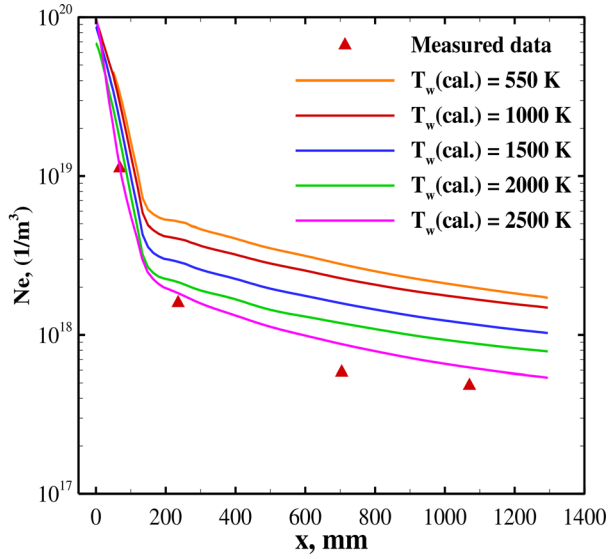

(a) Altitude of 61 km

(b) Altitude of 71 km

FIG. 13. Comparison of the electron number density along the RAM-C-II wall with different wall temperatures set in the simulations at (a) altitude of 61 km and (b) altitude of 71 km.

along the vehicle wall to the stagnation point, and T_w represents the wall temperature setting in the simulations. By comparing the results at the two altitude cases, the overall trend and magnitude of the calculated results for different wall temperatures agree with the experimental values, with a maximum error of no more than one magnitude. It is also found that the electron number density calculated for the different wall temperatures differs despite the same altitude case. As the wall temperature increases, the electron number density gets closer to the experimental value. This may be because the higher the wall temperature, the more intense the chemical reactions in the flow field near the wall, resulting in the number of electrons generated being closer to the actual value. Essentially, the vehicle wall temperatures are considered constant in the numerical simulations. In contrast, the reality is that the temperatures on different walls of the vehicle vary from time to time, making it difficult to determine the actual value of the wall temperature. The setting method is one of the vital factors influencing the reentry environment prediction. So, further study on the accurate computational method of the wall temperature of a reentry vehicle might be performed in future to reveal the effect of the wall boundary condition on the flow-field numerical results of a hypersonic reentry aircraft.

V. CONCLUSIONS

In this study, the non-equilibrium flow-field characteristics of the plasma sheath around the ARD were studied at different altitudes. A multi-physics numerical model developed in this study was used as an efficient computational method for simulating the plasma flow around a hypersonic vehicle. The numerical results obtained could provide basic data and theoretical guidance for revealing the characteristics of the plasma sheath and the aerodynamic heating of the reentry vehicle. In summary, the following conclusions are obtained from this study:

Inside the shock wave, the dominant chemical species are N, O, and N_2. A strong thermal non-equilibrium phenomenon occurs at 85 km, but the plasma flow tends to be in local thermal equilibrium at 65 km. The flow temperature decreases rapidly near the vehicle wall, and the molar fraction of N_2 and O_2 increases slightly. As the free stream passes through the shock layer, the gas pressure increases rapidly and eventually reaches a maximum near the vehicle wall. The high-pressure region of the wall is concentrated near the head of the vehicle. The wall pressure decreases rapidly in the rear cone and rear cover section of the vehicle. The distance from the shock layer to the stagnation point decreases with a decrease in the reentry altitude from 90 to 65 km, but increases with a decrease from 65 to 40 km. The electron number density in the shock layer is the highest, but in the wake region, it differs significantly at different flight altitudes. RF blackout occurs from 80 to 65 km. The ARD is completely blocked in the region where the electron number density exceeds the critical value, while the electron number density increases with decreasing altitude.

The 54 chemical-reaction model of air considers more associative ionization reactions and more electric charge exchange reactions relating to NO and NO^+ than the 49 chemical-reaction model. The 54-reaction model has higher numerical accuracy in predicting air chemical concentrations, and simulates the plasma sheath environment of hypersonic reentry vehicles more realistically. The variation trend and magnitude of the calculated results from the numerical model presented in this study agree with the experimental data, with a maximum error of no more than one magnitude. The different setting of the

vehicle wall temperature influences the electron number density significantly near the wall.

ACKNOWLEDGMENTS

This study was funded by the National Natural Science Foundation of China (Grant No. 12175177) and Jiangxi Key Laboratory for Aircraft Design and Aerodynamic Simulation, Nanchang Hangkong University, People's Republic of China (Grant No. EI202280265). All calculations were conducted on the Tianhe II supercomputer at National Supercomputing Center in Guangzhou, China.

AUTHOR DECLARATIONS

Conflict of Interest

The authors have no conflicts to disclose.

Author Contributions

Minghao Yu: Conceptualization (equal); Formal analysis (equal); Methodology (equal); Software (equal); Writing – original draft (equal); Writing – review & editing (equal). **Zeyang Qiu:** Data curation (lead); Investigation (equal); Writing – original draft (equal). **Bowen Zhong:** Funding acquisition (equal); Investigation (equal); Writing – review & editing (equal). **Yusuke Takahashi:** Conceptualization (equal); Investigation (equal); Methodology (equal); Software (lead); Writing – review & editing (equal).

DATA AVAILABILITY

The data that support the findings of this study are available from the corresponding authors upon reasonable request.

REFERENCES

[1]M. Gong, J. Tan, D. Li, Z. Ma, G. Tian, J. Wang, and L. Meng, "Review of blackout problems of near space hypersonic vehicles," J. Astronaut. **39**, 1059–1070 (2018).
[2]J. Wang, X. Yang, Y. Jing, and S. You, "On the communication blackout during reentry of blunt-nosed spacecraft and its eliminating approaches," Spacecr. Eng. **23**, 6–16 (2014).
[3]M. Yu and Z. Qiu, "Review of blackout mitigation methods for vehicles during atmospheric reentry," Chin. Space Sci. Technol. **42**, 1–12 (2022).
[4]B. Parent, P. Rajendran, and A. Omprakas, "Electron losses in hypersonic flows," Phys. Fluids **34**, 016110 (2022).
[5]S. Deep and G. Jagadeesh, "Aerothermodynamic effects of controlled heat release within the hypersonic shock layer around a large angle blunt cone," Phys. Fluids **30**, 106103 (2018).
[6]W. Jones and A. Cross, "Electrostatic-probe Measurements of plasma parameters for two reentry flight experiments at 25000-feet-per-second," Report No. NASA-TN-D-6617 (National Aeronautics and Space Administration, 1972).
[7]M. Golombek, "The Mars Pathfinder mission," J. Geophys. Res. **102**, 3953–3965, https://doi.org/10.1029/96JE02805 (1997).
[8]H. Lin and Z. Zhao, "The atmospheric reentry demonstrator," Spacecr. Recovery Remote Sens. **17**, 1–9 (1996). (in Chinese).
[9]R. Gupta, J. Moss, and J. Price, "Assessment of thermochemical nonequilibrium and slip effects for orbital reentry experiment," J. Thermophys. Heat Transfer **11**, 562–569 (1997).
[10]G. Tchuen and D. Zeitoun, "Computation of weakly ionized air flow in thermochemical nonequilibrium over sphere–cones," Int. J. Heat Fluid Flow **29**, 1393–1401 (2008).
[11]Y. Takahashi and K. Yamada, "Aerodynamic-heating analysis of sample-return capsule in future trojan-asteroid exploration," J. Thermophys. Heat Transfer **32**, 547–559 (2018).
[12]Y. Takahashi, K. Yamada, T. Abe, and K. Suzuki, "Aerodynamic heating around flare-type membrane inflatable vehicle in suborbital reentry demonstration flight," J. Spacecr. Rockets **52**, 1530–1541 (2015).
[13]Y. Takahashi, T. Ohashi, N. Oshima, Y. Nagata, and K. Yamada, "Aerodynamic instability of an inflatable aeroshell in suborbital re-entry," Phys. Fluids **32**, 075114 (2020).
[14]R. Palharini, T. Scanlon, and C. White, "Chemically reacting hypersonic flows over 3D cavities: Flowfield structure characterisation," Comput. Fluids **165**, 173–187 (2018).
[15]S. Surzhikov, "Spatial ionization effects of a shock layer in the RAM-C-II flight experiment," Dokl. Phys. **60**, 89–94 (2015).
[16]M. Jung, "Numerical study of plasma flows and radio frequency blackout for reentry vehicle," Ph.D. thesis (Kyushu University, 2018).
[17]Y. Du, S. Sun, M. Tan, Y. Zhou, X. Chen, X. Meng, and H. Wang, "Non-equilibrium simulation of energy relaxation for earth reentry utilizing a collisional-radiative model," Acta Astronaut. **193**, 521–537 (2022).
[18]M. Liu, "Numerical simulation of an apollo like reentry capsule," M.S. thesis (Harbin Institute of Technology, 2013).
[19]J. Hao, J. Wang, Z. Gao, C. Jiang, and C. Li, "Numerical simulation of electronic-electron energy nonequilibriumin high speed and high temperature flowfields," Acta Aeronaut. Astronaut. Sin. **37**, 3340–3350 (2016).
[20]R. Liang, "Numerical simulation of the flow field and radiative properties for hypersonic vehicle in high-temperature environment," M.S. thesis (Xidian University, 2019).
[21]T. Leveugle and D. Reinhard, "The atmospheric reentry demonstrator(ARD): A successful recovery at sea," in 15th Aerodynamic Decelerator Systems Technology Conference, 1999.
[22]M. Yu, Z. Qiu, B. Lv, and Z. Wang, "Numerical simulation of the thermal non-equilibrium flow-field characteristics of a hypersonic Apollo-like vehicle," Chin. Phys. B **31**, 094702 (2022).
[23]Y. Takahashi, N. Enoki, H. Takasawa, and N. Oshima, "Surface catalysis effects on mitigation of radio frequency blackout in orbital reentry," J. Phys. D **53**, 235203 (2020).
[24]J. Huba, *NRL Plasma Formulary* (Naval Research Laboratory, 2004).
[25]C. Curtiss and J. Hirschfelder, "Transport properties of multicomponent gas mixtures," J. Chem. Phys. **17**, 550–555 (1949).
[26]R. Gupta, J. Yos, and R. Thompson, "A review of reaction rates and thermodynamic and transport properties for an 11-species air model for chemical and thermal nonequilibrium calculations to 30000 K," Report No. NASA-RP-1232 (National Aeronautics and Space Administration, 1990).
[27]J. Yos, "Transport properties of nitrogen, hydrogen, oxygen, and air to 30000 K," Report No. TRAD-TM-63-7 (National Aeronautics and Space Administration, 1963).
[28]R. Devoto, "Simplified expressions for the transport properties of ionized monatomic gases," Phys. Fluids **10**, 2105 (1967).
[29]S. Ghorui and A. Das, "Collision integrals for charged-charged interaction in two-temperature non-equilibrium plasma," Phys. Plasmas **20**, 093504 (2013).
[30]M. Yu, H. Kihara, K. Abe, and Y. Takahashi, "Computation and analysis of the electron transport properties for nitrogen and air inductively-coupled plasmas," J. Korean Phys. Soc. **66**, 1833–1840 (2015).
[31]T. Mankodi and R. Myong, "Quasi-classical trajectory-based non-equilibrium chemical reaction models for hypersonic air flows," Phys. Fluids **31**, 106102 (2019).
[32]M. Yu, W. Wang, J. Yao, and B. Zheng, "A chemical kinetic model including 54 reactions for modeling air nonequilibrium inductively coupled plasmas," J. Korean Phys. Soc. **73**, 1519–1528 (2018).
[33]C. Park, "Review of chemical-kinetic problems of future NASA missions. I—Earth entries," J. Thermophys. Heat Trans. **7**, 385–398 (1993).
[34]M. Dunn and S. Kang, "Theoretical and experimental studies of reentry plasmas," Report No. NASA-CR-2232 (National Aeronautics and Space Administration, 1973).
[35]M. Yu, "Numerical investigation on interaction mechanisms between flow field and electromagnetic field for nonequilibrium inductively coupled plasma," Acta Phys. Sin. **68**, 185202 (2019).
[36]M. Gallis and J. Harvey, "The modeling of chemical reactions and thermochemical nonequilibrium in particle simulation computations," Phys. Fluids **10**, 1344 (1998).

[37]C. Park, R. Jaffe, and H. Partridge, "Chemical-kinetic parameters of hyperbolic earth entry," J. Thermophys. Heat Transfer **15**, 76–90 (2001).
[38]C. Park, "Rotational relaxation of N_2 behind a strong shock wave," J. Thermophys. Heat Transfer **18**, 527–533 (2004).
[39]R. Millikan and D. White, "Systematics of vibrational relaxation," J. Chem. Phys. **39**, 3209–3213 (1963).
[40]S. Lazdinis and S. Petrie, "Free electron and vibrational temperature nonequilibrium in high temperature nitrogen," Phys. Fluids **17**, 1539 (1974).
[41]W. Vincenti, C. Kruger, and J. Teichmann, "Introduction to physical gas dynamics," Phys. Today **19**(10), 95 (1966).
[42]J. Appleton and K. Bray, "The conservation equations for a non-equilibrium plasma," J. Fluid Mech. **20**, 659–672 (1964).
[43]P. Gnoffo, R. Gupta, and J. Shin, "Conservation equations and physical models for hypersonic air flows in thermal and chemical nonequilibrium," Report No. NASA-TP-2867 (National Aeronautics and Space Administration, 1989).
[44]J. Liu, "Numerical simulation of the flow field of a three-dimensional chemical non-equilibrium flow in the return capsule," MS. thesis (National University of Defense Technology, 2000).
[45]M. Jung, H. Kihara, K. Abe, and Y. Takahashi, "Numerical analysis on the effect of angle of attack on evaluating radio-frequency blackout in atmospheric reentry," J. Korean Phys. Soc. **68**, 1295–1306 (2016).
[46]B. Parent, "Electron heating and cooling in hypersonic flows," Phys. Fluids **33**, 046105 (2021).